Received April 9, 2022, accepted May 3, 2022, date of publication May 9, 2022, date of current version May 17, 2022.

Digital Object Identifier 10.1109/ACCESS.2022.3173176

Quickly Convert Photoplethysmography to Electrocardiogram Signals by a Banded Kernel Ensemble Learning Method for Heart Diseases Detection

WEN-HSIEN HO[1,2,3], CHIA-TE LIAO[4,5,6], YENMING J. CHEN[7], KAO-SHING HWANG[1,8], AND YANYUN TAO[9]

[1]Department of Healthcare Administration and Medical Informatics, Kaohsiung Medical University, Kaohsiung 80708, Taiwan
[2]Department of Medical Research, Kaohsiung Medical University Hospital, Kaohsiung 80708, Taiwan
[3]Department of Mechanical Engineering, National Pingtung University of Science and Technology, Pingtung 91201, Taiwan
[4]Division of Cardiology, Chi Mei Medical Center, Department of Internal Medicine, Tainan 710, Taiwan
[5]Studies Coordinating Centre, KU Leuven Department of Cardiovascular Sciences, Research Unit Hypertension and Cardiovascular Epidemiology, University of Leuven, 3000 Leuven, Belgium
[6]Department of Public Health, College of Medicine, National Cheng Kung University, Tainan 710, Taiwan
[7]Department of Information Management, National Kaohsiung University of Science and Technology, Kaohsiung 81164, Taiwan
[8]Department of Electrical Engineering, National Sun Yat-sen University, Kaohsiung 81164, Taiwan
[9]Institution of Intelligence Structure and System, Soochow University, Suzhou 215006, China

Corresponding authors: Chia-Te Liao (drctliao@gmail.com) and Yenming J. Chen (yjjchen@nkust.edu.tw)

This work was supported in part by the Chi-Mei Medical Center; in part by the Kaohsiung Medical University Research Foundation under Grant 109CM-KMU-013; in part by the Ministry of Science and Technology, Taiwan, under Grant MOST 108-2221-E-037-007 and Grant MOST 109-2410-H-992-018-MY2; in part by the NSYSU-KMU Joint Research Project under Grant NSYSUKMU 110-P014; and in part by the Intelligent Manufacturing Research Center (iMRC) through the Featured Areas Research Center Program within the Framework of the Higher Education Sprout Project by the Ministry of Education (MOE) in Taiwan.

ABSTRACT Electrocardiography (ECG) is generally deemed the golden standard for diagnosing cardiovascular diseases and photoplethysmography (PPG) is unobtrusive, low-cost, and convenient for continuous monitoring. However, PPG contains insufficient information to diagnose diseases. In this study, we propose a novel method to accurately convert PPG to ECG. The banded kernel ensemble method converts a low-quality source (PPG) to a high-quality destination (ECG). Unlike neural network solutions, our algorithm requires no computation burden in the conversion task after a trained model is obtained. The proposed algorithm is then tested on a publicly available MIMIC III database. Our prediction shows excellent accuracy in the validation dataset. It offers the testing performance of under 0.314 and above 0.55 in rrmse (relative root mean squared error) and KGE (Kling–Gupta efficiency), respectively, under the scenarios of three prevalent heart diseases. The reconstructed ECG can be further used to perform heart disease detection and we obtained an average correctness rate of 81%. Our method can help a large population of high-risk, believed-healthy persons to walk into doctors' offices before the situation becomes irreversible.

INDEX TERMS Photoplethysmography (PPG), electrocardiogram (ECG), complex wavelets, banded kernel ensemble method, successive ridge domination (SRD), generative pulse locking (GPL).

I. INTRODUCTION

EElectrocardiography (ECG) is the top preferred option for diagnosing cardiovascular diseases. This knowledge is also an essential part of the training of every medical student. However, detecting minute electrical currents on skin surfaces requires relatively expensive equipment operated by a professional. Therefore, monitoring cardiac activities for a healthy person by maintaining the wiring on for an extended period in a daily living space is difficult. Alternatively, non-contact photoplethysmography (PPG) is considered unobtrusive, low-cost, and convenient for continuous monitoring. PPGs are usually deemed low quality with random drifts. Consequently, the majority of PPG applications can only be

The associate editor coordinating the review of this manuscript and approving it for publication was Gyorgy Eigner.

applied to simple tasks, such as heart rate counting, thereby producing low values in clinical applications.

In this study, pervasive PPG signals, such as the ones from wristwatches or PPG imaging, are utilized to synthesize corresponding ECG signals (Fig. 1). Differing from those wiring devices, such as AppleWatch ® [1] or AliveCor ® [2], our solution does not need to prepare a clean contact or using both hands to acquire weak electric signals. Therefore, suspicious cardiology symptoms can be detected unobtrusively and ubiquitous, and the consequent early hospitalization can save many lives. The framework addresses the ill-posed inverse problem by applying a hybrid learning technique over a multi-band time-frequency domain with successive ridge domination (SRD) and generative pulse locking (GPL) algorithms.

We concentrate on PPGs because the device is low-cost and ubiquitous. PPG has a wide range of applications, from human physiology to psychology, because of its low-cost, ubiquitous, and unobtrusive nature. For example, PPG has been applied to vital sign monitoring [3], [4]. In professional sports training, simple PPG devices are apt to record history and optimize performance in the field [3]. In psychology, PPG can help humans outside laboratories understand stress responses and emotional communication [3], [5]. Despite the quality of the devices, recent advancement demonstrates a promising result in the accurate measurement of specific physiological parameters, e.g., estimating blood pressure from PPG based on specific haemodynamics [6].

Among PPG applications, medical diagnosis is scant, whereas the commonly used device is ECG [7], [8]. However, ECG devices require a good touch of electrodes on human skin, causing skin irritation and discomfort during long-term usage. As such, most consumer-grade products only perform occasional measures instead of continuous monitoring. For example, the wrist-worn Apple Watch can only collect signals when fingers touch the wristwatch [1]. Another consumer product, KardiaMobile, completely overlaps the market positioning with Apple Watch [2]. Other laboratory-grade products, such as a single-use patch with a 7-day lifespan [9] and a textile-based printed circuit in cloth [10], probably still need to overcome certain usability problems at the current stage.

This study offers a unique contribution that fills the current research gaps described in the existing literature. First, our hybrid band method can recover ECGs reliably at low bands without requiring a high-quality PPG input. This feature is essential because signals collected in a living space cannot guarantee good acquisition quality. Additionally, ECG information can be reserved at high-bands without affecting the stability of the recovery. The learning ensemble can adapt to different situations while maintaining the fundamental characteristic of ECGs because various heart activities reflect diversified PPG and ECG patterns. This feature fills a gap of not being capable of diagnosing PPG inputs. Therefore, doctors can automatically assess the heart condition of ordinary people through long-term surveillance in daily life.

II. RELATED WORKS

Research gaps exist in the existing literature. Although ill-posed problems have been studied for a long time, a large amount of active research keeps shedding new light in the field. Recently, approaches of optimization on l_1 have proven effective. Two strategies are usually applied to the inverse mapping problem [15]. Certain implicit constraints, such as smoothness or sparseness, can be imposed. Dimension reduction, such as the kernel-based method, can be applied. If the back-projection problem satisfies specific sparsity properties, the optimization, therefore, receives additional constraints [23]. Sparse domain techniques have been widely used in heart rate activity monitoring [32]. The space that possesses good sparsity is the one with time-frequency representation [33], [34]. Optimization performed on such multi-resolution space is considered effective [16].

The conversion from PPGs to ECGs has a solid theoretic ground in modern physiology. Studies have supported the relationship between PPG and ECG in electro-mechanics and blood fluid dynamics in heart activities. The transmembrane potential distribution can be constrained by a diffusion-reaction model from cellular activation dynamics [11]. The electric current constraints from the ionic behavior of the individual cell, such as in [12], impose additional computational challenges due to millions of myocytes. Additionally, additional constraints also introduce more unknown parameters and the degree of freedom remains still high. However, a numerical problem exists because ECG signals contain more details than PPG signals do. To deal with the problem that physiological models and patient-specific body surface electrical data are always corrupted by noise and organ geometries may be constructed incorrectly. The inverse mapping problem reversely describes ECG, haemodynamics, and electro-fluid-mechanics in differential equations [11], [13], [14]. Therefore, reconstructing ECGs without involving differential equations is challenging.

Solving the ill-posed inverse problem that maps the surface ECG to the transmembrane potentials on the surface of the heart, the key adequately constrains the solution space to obtain a unique solution. Unfortunately, most regulation methods in the ill-posed situation can only condition the numerical difficulty from a mathematical point of view. However, the problem of multiple solutions must be addressed by restoring possible missing constraints. Continuous basis pursuit has been reported effective for sparse spike reconstruction in the sense of super-resolution [24]. In addition to sparsity constraints, other constraints, such as total variation with positivity constraint [25], smoothness on low-dimensional manifolds [26], constraints on the union of all subspaces [27], and block-sparsity constraints [28], have also proven effective.

The first attempt at the PPG-related problems starts from an easy one that reduces ECGs to PPGs, which only involves mapping from high to low dimensions [35]. Recently, many studies have reported success for the challenged ill-posed

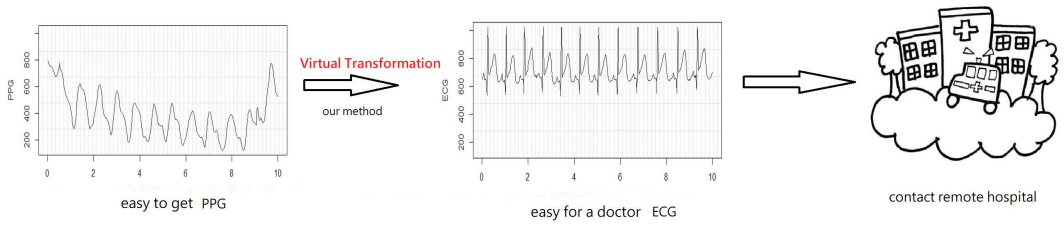

FIGURE 1. Usage scenario for PPG–ECG transformation in a wearable device providing medical assistance in daily life.

TABLE 1. A summary with previous studies and research gaps.

Research topic	Current progress	Current gap	Our solution
Physiological relations	Electro-fluid-mechanics from transmembrane to hemoglobin density [11, 12, 13, 11, 14, 15]	Solving differential equations is time-consuming	Machine learning
PPG-ECG solutions	Statistics [16, 17, 18, 19, 20, 21, 22, 17] Neural networks [18, 19, 20, 21, 22]	Computation and stability issues	Banded kernel ensemble
	Sparse space projection [23, 24, 25, 26, 27, 28]	Sensitive to input quality	Generative method
Ill-posed mapping	Long-memory functionals [29, 30, 31]	Losing details	Band separation
	Neural networks [19, 20, 21, 22]	Time consuming	Matrix transformation
	Regression [17, 18].	Not adaptive	Adaptive band boosting

inverse problem. For the back projection from PPGs to ECGs, an ordinary regulation on l_2 can only solve a part of numerical difficulty [17], [18]. Many studies resort to neural networks to bypass mathematical details [19]–[22]. The neural network approaches utilize a latent space in the auto-encoder or generative adversarial network framework, which is akin to the concept of partial least square. The key to these approaches is a proper design of the loss function, but they do not take advantage of the sparsity of ECG signals in l_1 space. Our study further improves the numerical ill-posedness and the wide tolerance of the quality of source PPGs.

A previous study takes a statistical approach but they need to know the subject's personal information in the regression and the input and output should be properly aligned; therefore pulse timing information is lost [17]. In another study, a compressive sensing technique is employed to improve the signal reconstruction [18]. However, the study has yet to clarify how discrete cosine transform and dictionary decomposition-based methods can resist the non-coherency distortion on PPGs. The recent neural network studies have achieved excellent progress, but they have yet to discover how the black box algorithm can handle low-quality PPGs and signals with disease patterns [19]–[22]. The massive computation of deep computation is also difficult to implement on consumer devices, such as smartphones [36].

Long-memory and fractal properties, such as coherency, usually exist between two time-series, particularly in the heart signals. That is, the coherency reflects the similarity between the semi-periodic heart activities. However, the coherency properties may change even within the proximal scale. Therefore, we should develop an elaborate method to estimate the model and ensure that the realizations of a stochastic process can correctly express the model. Therefore, a functional time series is a mathematical structure where the entire function becomes a value in Hilbert space [37]. We vectorize the signals into a functional time series such that the reconstructed signals depend not only on the immediate successors but also on the repetitive patterns of the previously reconstructed heartbeats. A functional time series possesses the advantage of modeling the long-range correlation in a semi-periodic wave. Therefore, the evolution of the continuous-time stochastic process of heart signals can be easily parametrized in a representative model.

Functional time series have long been investigated for the coherency property. A subgroup covariance structure can be determined in functional auto-regression [29]. The coherency structure is proven effective in improving the performance of prediction [30]. The functional correspondence can also be effectively obtained through a matrix completion [31]. Therefore, our method also takes advantage of the coherency structure for the optimization of functional time series and swiftly reconstructs a high fidelity ECG. By upgrading the PPG to ECG, the automatic diagnosis of heart diseases can be performed in the consequence.

III. BANDED KERNEL ENSEMBLE METHOD

PPG signal $s(t)$ and ECG signal $z(t)$ originate from the same driving source but transmit through different media. Therefore, they should be similar in certain subspaces but dissimilar in other subspaces. The signal $z(t)$ contains rich information, including smooth and non-smooth components. The versatile similarities and ill-posedness in each subspace

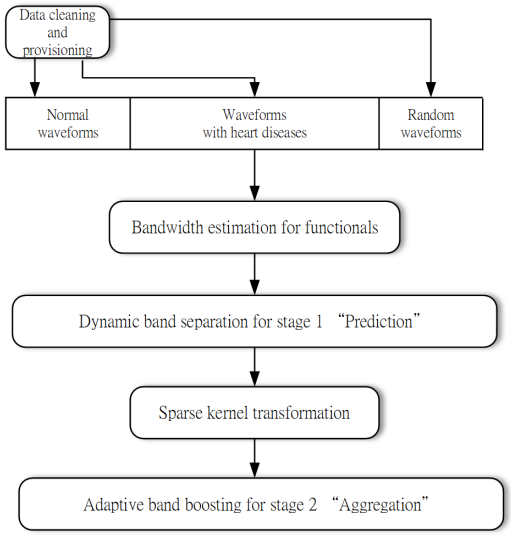

FIGURE 2. An ensemble of methods in two-stage prediction.

should be treated differently. In certain smooth subspaces, an ordinary pseudo-inverse in l_2 is sufficient to reconstruct the signal. However, some components in ECG signals are difficult to handle and some extremely non-smooth ones must take special treatment in the destination manifolds.

A typical technique to solve an ill-posed problem is adding certain constraints with prior knowledge of the sparsity or smoothness in the original signals. However, no single set of constraints can perfectly solve the ill-posed problem at once. Appropriate methods should be applied to each subspace to pursue the most stable transformation results with different constraint sets. We need to decompose the signals to individual components in a particular subspace that inhere the prior knowledge. Multiple methods in the ensemble method are then applied to maximize and validate the accuracy of prediction. We develop an ensemble of methods in a series of operations (Fig. 2). Our algorithm will find the best learner for each subspace in the inverse mapping.

In Fig. 2, with the original signal pair $(z(t), s(t))$ for ECG and PPG, we first transform the waves to banded functional pairs $(Y, X) = (Y_{b,i}(t), X_{b,i,k}(t)) = (z_b(t + (i-1)n), \langle s_b(t + (i-1)n), \Psi_k\rangle)$, where $b = 1, \ldots, B$, $i = 1, \ldots, M$, $k = 1, \ldots, K$, and $t \in [\underline{t}, \bar{t}]$ for B bands, K kernels, M functional chunks with bandwidth n, respectively for using the kernel function Ψ_k. The subscription b in $z_b(t)$ represents that the original signal $z(t)$ has been separated into $b = 1, \ldots, B$ bands. The kernel operator for predictor functionals $\langle \cdot, \cdot \rangle$ is defined in the Hilbert space such that the informative projection is prominent. We choose the kernel function $\Psi_k = \Psi_k(t, t') = k^{-1} e^{-\gamma ||(t-t')/k||^2}$ for $t' \in [\underline{t}, \bar{t}]$ with a parameter γ such that the operator is given as $\langle s_b(t + (i-1)n), \Psi_k \rangle = \int s_b(t' + (i-1)n) k^{-1} e^{-\gamma ||(t-t')/k||^2} dt'$.

We apply the functional kernel estimator (1) in accordance with previously described method to determine the functional bandwidth n [38].

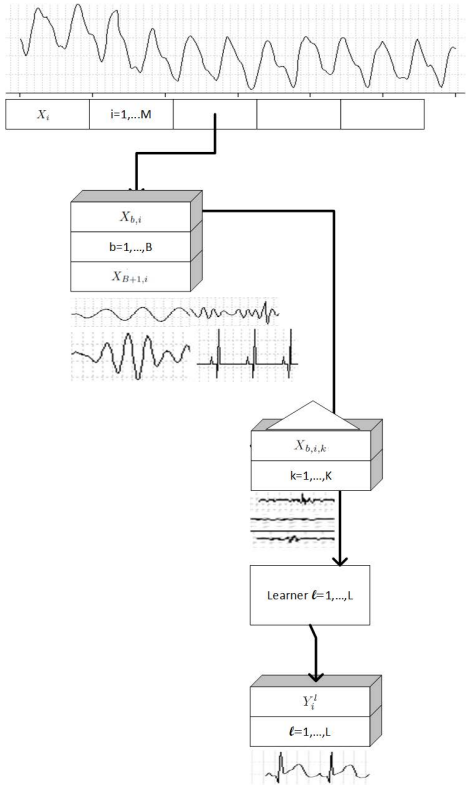

FIGURE 3. The detailed stage-1 process that breaks down the functional X to the basic process unit $X_{b,i,k}$ for $b = 1, \ldots, B$, $i = 1, \ldots, M$, $k = 1, \ldots, K$, and $t \in [\underline{t}, \bar{t}]$ for B bands, K kernels, M functional chunks with bandwidth n. All the basic process unit $X_{b,i,k}$ will send to each learner in the ensemble and produce Y_i^l for learner $l = 1, \ldots, L$.

Let the process $X_{b,i,k}(t_j)$ satisfies a Hilbert-valued autoregressive process $X_{b,i+1,k}(t_j) = m(X_{b,i,k}(t_j), t_j) + \epsilon_i$, where ϵ_i is a Gaussian noise and $m(x_d, t_j) = \mathrm{E}[X_{b,i+1,k}(t_j) | X_{b,i,k}(t_j) = x_d]$, $j = 1, \ldots, N_t$ with the expectation E.

The sampling $(x_d)_{d=1,\ldots,N_d}$ is the realization sequence of a discrete-time stochastic process $X_{b,i,k}(t_j)_{j=1,\ldots,N_t}$. The estimation $\hat{m}_n(x_d, t_j)$ in Eq. (1) can be deemed a functional generalization of the Nadaraya-Watson regression estimator at any point x_d and time t_j for $d = 1, \ldots, N_d$ and $j = 1, \ldots, N_t$ with sampling sizes N_d and N_t, which gives the preceding data points more weight.

$$\hat{m}_n(x_d, t_j) = \frac{\sum_{i=1}^{n-1} \langle X_{b,i,k}(t_j) - x_d, \Psi_k \rangle X_{b,i+1,k}(t_j)}{\frac{1}{n} + \sum_{i=1}^{n-1} \langle X_{b,i,k}(t_j) - x_d, \Psi_k \rangle}. \quad (1)$$

To determine the bandwidth n, we perform a grid search such that the square error $\sum_{\forall d,j} \mathrm{E}[m(x_d, t_j) - \hat{m}_n(x_d, t_j)]^2$ is minimized.

At the first stage prediction, the back projection $X \mapsto Y$ problem reduces to a standard form (2) that the parametric $f(\cdot)$ and the covariance matrix ϵ are estimated simultaneously.

$$Y = f(X) + \epsilon, \quad (2)$$

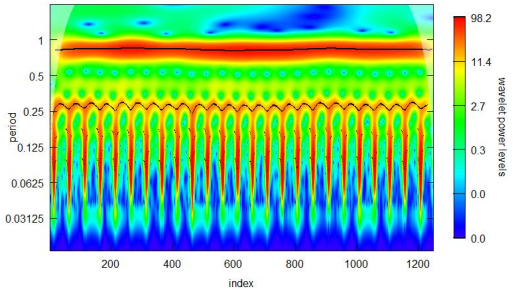

(a) CWT of ECG

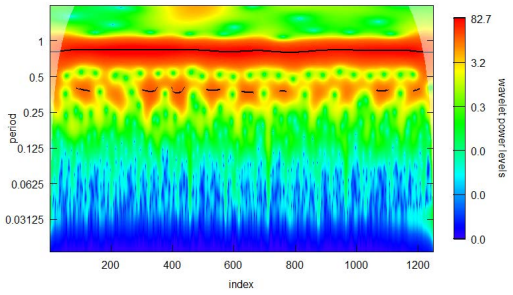

(b) CWT of PPG

FIGURE 4. Continuous wavelet transformations (CWT) of ECG (upper panel) and PPG (lower panel) waves.

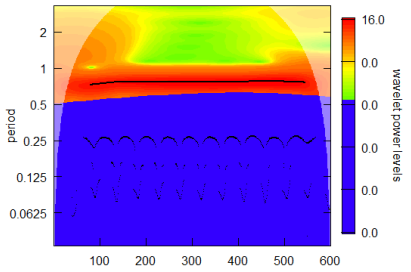

(a) low-band

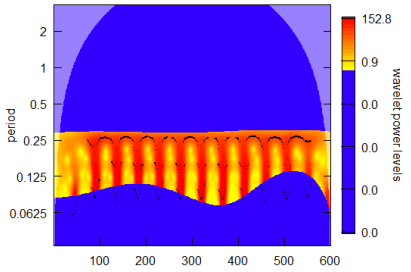

(b) mid-band

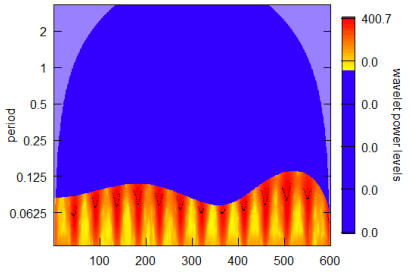

(c) high-band

FIGURE 5. The number of bands can be elected to adapt to real applications. Successive ridge domination (SRD) dynamically decomposes an ECG wave into three bands. The vertical axis represents the number of seconds for a cycle; a period 0.25 corresponds to 4 Hz. The horizontal axis denotes the sampling index; point 1200 corresponds to 9.6 seconds for the 125Hz sampling rate.

where the functional pair (Y, X) represent the collection of $Y_{b,i}(t)$ and $X_{b,i,k}(t)$ for the b-th band and k-th kernel within the point i of frame t. The predicted functionals from each band at the second stage will be aggregated together into a single one through an adaptive band-boosting step.

A. DYNAMIC BAND SEPARATION AT THE FIRST PREDICTION STAGE

In the detailed operation at the first stage, as shown in Fig. 3, functionals have been separated into bands for a suitable prediction algorithm. The basic process unit $X_{b,i,k}$ has been sent to the learners in the stage 1 prediction process. The proposed successive ridge domination (SRD) splits signals into multiple bands dynamically according to their dominated wavelet ridges in the time-frequency domain.

In Fig. 4, taking a sample of PPG and ECG signals, we depict their continuous wavelet for an any function $w(\tau)$ such that the wavelet transform is defined as $W_w(a,t) = \int \frac{1}{\sqrt{a}}\xi\left(\frac{\tau-t}{a}\right) w(\tau)d\tau$, with mother wavelet ξ performing dilation in scale a and shift in scale t.

The time-frequency representation easily reflects the local properties of the signal in the coefficients. For example, the continuous wavelet transformations (CWT) of the ECG in Fig. 4 indicated that the base frequency of heartbeats is around the period of 1 second (or 60 beats per minute). The vertical axis in the graph represents the frequency in a log scale from the top 0.5 Hz to the bottom 30Hz.

To compute ridge points over the time-frequency representation, we need to define ridge curves. An amplitude ridge point and phase ridge point is the time/scale pair (a,t) with the strictly local maximum of $\Re\{\ln|W_w(a,t)|\}$ and $\frac{\partial}{\partial t}\Im\{\ln|W_w(a,t)|\}$ along the a and t axes, respectively, where the operators $\Re$ and $\Im$ retrieve the real and image part of a complex number, respectively, and $W_w(a,t)$ is a wavelet transform of an any function $w(\tau)$. In other words, amplitude ridge points are defined as $\arg\max_{(a,t)}\Re\{\ln|W_w(a,t)|\}$. The sets of ridge points collectively become wavelet ridge curves. As depicted in Fig. 5, we split the bands based on the ridge curves. The ridge amplitudes are prominent in components around the vicinity of heart rates because of the semi-periodic nature of cardiac activities.

Therefore, we successively cut the components in the low band and evaluate the next dominated ridge over the residual coefficients.

The first subgraph in Fig. 5 is the band with the most dominated ridges, and the second subgraph becomes the successive

dominated ridges. The time-frequency representation (a, t) forms some Riemannian submanifold $\mathcal{M}$ of $\mathbb{R}^{m\times n}$. A manifold is a space having no global coordinate systems. However, locally at a point $X \in \mathcal{M}$, the manifold is homeomorphic to a Euclidean space.

Therefore, we utilize the manifold to extend the residual subspace for accommodating possible hidden details. The components in the final band belong to non-smooth manifolds $\mathcal{S}_x$ and $\mathcal{S}_y$ for PPG and ECG. For the simplicity and consistency of notations, we still use the same X and Y to denote the non-differentiable functional in the non-smooth manifold.

The non-smooth manifolds $\mathcal{S}_x$ and $\mathcal{S}_y$ for signals X and Y are defined on a lattice of Laplacian Δ, representing an $n \times n$ matrix. Let a functional correspondence $\mathcal{T} \in \mathbb{R}^{n\times n}$ maps functions from Lebesgue space $L^2(\mathcal{S}_x)$ to $L^2(\mathcal{S}_y)$. The functional correspondence $\mathcal{T}$ can be approximated by the first k Laplacian eigenvectors as $\mathcal{T} \approx \Phi_x W_w(a, t)\Phi_y^T$ in a sense subgradient, where $W_w(a, t)$ is a $k \times k$ matrix translating Fourier coefficients from the basis Φ_x to the basis Φ_y.

To avoid "contaminating" the good properties of components in the smooth manifolds, we keep extracting all low-frequency smooth components according to the dominated wavelet ridges until reaching the final components, which are highly irregular and have sparse spikes. The final components cannot be discarded as noises because the mapping between the components determines the quality details of the destination signals. The estimation of the mapping function in the manifold is challenging because of the no-where differentiable property. However, a good estimation in the non-smooth manifold is key to the inverse project in our target problem.

The filter bank obtained by our SRD algorithm guarantees a well-separation of heart activities, and the reconstructed waveform is loss-less (Fig. 6). We tried to demonstrate the difference between 3-band and 4-band decomposition. Fig. 6 graph shows the result of 4-band, which has no significant difference from the previous 3-band decomposition. We, therefore, choose to use 3-band decomposition hereinafter. The back-projection learning task in the first stage is an optimization process that evaluated the solutions to the ill-posed problem in each band b.

Considering that the application scenarios of wearable devices need to be accommodated to ordinary people's daily activities, the processing algorithm should overcome signals with a large portion of noise and artifacts. Wavelet methods are well-known for their excellent capability in removing non-coherent noises, artifacts, and drifting. Therefore, our SRD band splitting algorithm can obtain separated manifolds and rectify the input signals to an acceptable quality.

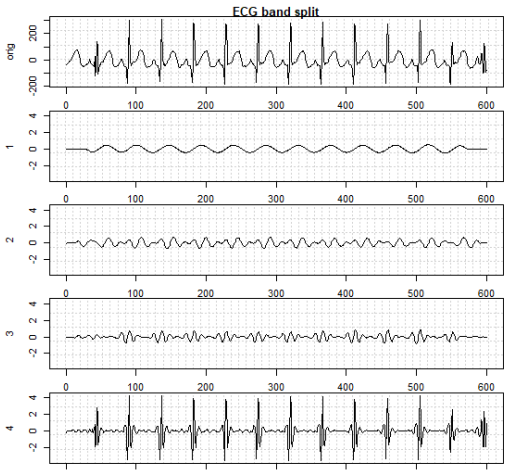

(a) ECG bands

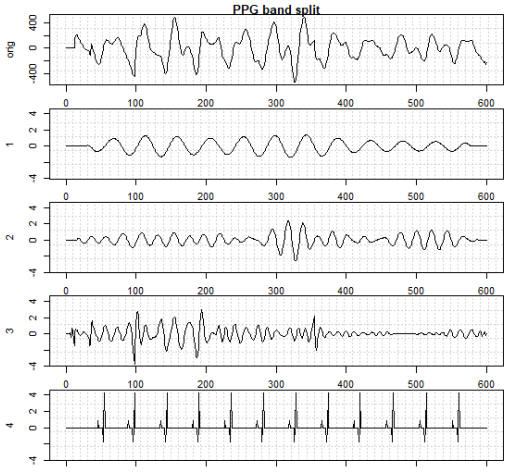

(b) PPG bands

FIGURE 6. Decomposed bands of ECG and PPG signals. (a) and (b) show the 4-band decomposition (1-4) of the original signal (orig). In choosing 3-band or 4-band decomposition, this graph shows that the result of 4-bands has no significant difference from the previous 3-band decomposition. We, therefore, choose to use 3-band decomposition hereinafter.

B. SPARSE KERNEL TRANSFORMATION FOR THE SOURCE PPG SIGNALS

Individual learner $l = 1, \ldots, L$ for the ensemble with L learners should adapt to the characteristics of each band. An effective way to highlight such characteristics is kernel transformation, Ψ_k [39]. The representer theorem in the reproducing kernel Hilbert space (RKHS) guarantees that, over the training set, the minimizer of the regularized minimization problem will find a functional g for a target functional s such that $\min_g ||s-g||^2 + \mu||g||_H^2$, $\mu \geq 0$, admits the representation $\hat{g}(X) = \sum_{k=1}^{n} \nu_k X_{b,i,k}(t))$ over a Hilbert space H, where $\nu_k \in \mathbb{R}^n$ denotes the unknown coefficients and μ is the Lagrange multiplier of the constraint.

The challenge of individual learners encountered in the ill-posed problem is to inverse a near-singular outer product, and it is often resolved through regularization methods with a positive perturbation. Therefore, the solution to the multivariate optimization problem becomes

$$\max_{\mu} \min_{g} ||s-g||^2 + \mu||g||_H^2. \tag{3}$$

To avoid over-fitting, we further generalize the problem (3) as a generic elastic net (4) in the Least Absolute Shrinkage and Selection Operator (Lasso) term [40] with Lasso penalty α with l_1 and l_2 norms, $||\cdot||_1$, $||\cdot||_2$.

$$\max_{\mu} \min_{g} ||s-g||^2 + \mu \left\{ \tfrac{1-\alpha}{2}||g||_2^2 + \alpha||g||_1 \right\}. \quad (4)$$

Optimization (4) pushes the coefficients to zero if the covariates are insignificant due to the l_1 properties. The reconstruction efficiency increases when transformation manifests the sparsity properties [41]. The optimization (4) is regulated by the Lasso penalty ($\alpha = 1$) or the ridge penalty ($\alpha = 0$), and it takes advantage of the sparse l_1 norm in evaluating solutions for the ill-posed problem [42]. If $\alpha = 0$, the optimization in (4) reduces to an ordinary generalized matrix inverse, which serves as a comparison basis. The least-square estimation in the objective creates a large variance when covariates exhibit multicollinearity. Ridge regression performs optimization to compensate for the problem of multicollinearity by finding a balance between variance and bias [43]. The ridge penalty effectively reduces the variance of the identified coefficients [44], [45].

C. GENERATIVE PULSE LOCKING FOR QRS COMPLEX

The mapping from PPG to ECG in high-frequency bands can be nearly singular because the PPG signals have insufficient high-frequency information. Instead of performing direct mapping, a generative method is exploited. Mirroring the concept of the phase-locked loop in radio communication, we estimate the transformation parameters based on a series of actively synthesized pulses from the low-bands of source PPGs (Fig. 7).

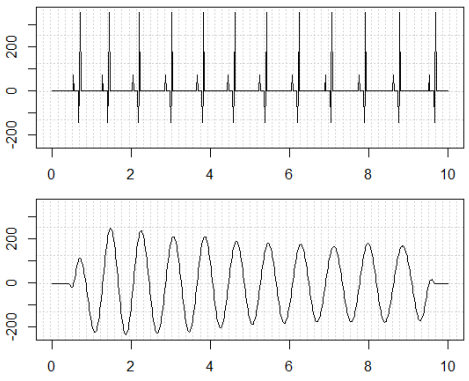

FIGURE 7. Generative pulse locking (upper panel) to simulate the QRS complex from low-bands of a PPG signal (lower panel).

The GPL pulses denoted as $X_{B+1,i}$, are synchronized with the reference band in phases and amplitudes by maximizing cross-correlation and minimizing the covariance error. The way we maximize and minimize the two objectives is consistent with the principle of generative methods in the recent renowned research [46]. The generative method can effectively overcome the numerical difficulty in the ill-posed inverse mapping.

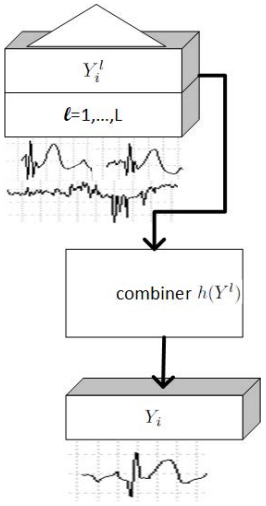

FIGURE 8. The detailed stage-2 process that combine the functional Y_i^l to the final ECG functional Y_i.

D. ADAPTIVE BAND BOOSTING AT THE SECOND AGGREGATION STAGE

At the second stage, as shown in Fig. 8, the multivariate regression (5) aggregate the predicted functionals Y_i^l, for which the superscript l of the Y (ECG) represents the output of the l-th learners in terms of the vectorized β_l, the combiner function $h(Y^l)$, and the independent residue η. The combined Y with combiner $h(Y^l)$ becomes

$$Y_i = \sum_{\forall l \in \text{the ensemble}} \beta_l h(Y_i^l) + \eta. \quad (5)$$

A numerical difficulty exists in (5) because multiple learners in the first stage increase the number of variables in multiple folds. While the un-trained records remain the same, the number of predictors is more than the number of observations in the regression. Therefore, ordinary regression fails in this case.

Conventional solutions usually involve specific transformations to reduce the dimension of predictors. For example, principal component analysis and partial least square (PLS) regression extract components with a significant variation in the covariance matrix of input and inputloutput, respectively. We exploit the sparse partial least square (SPLS) regression to further limit the number of predictors [47], [48]. In comparison with PLS, the SPLS effectively keeps response and predictors uncorrelated in the regression with a large number of predictors.

In a conventional PLS, Y and X are transformed by a matrix $V = XU \in \mathbb{R}^{n\times L}$, where L is the reduction dimension and U is the coefficient matrix. Many algorithms apply successive approach to solve V through finding each column vector in U. For example, simple partial least square (SIMPLS) [49] and multi-response SIMPLS [50] evaluate $U = \arg\max_U \{U^T \Sigma_{XY} \Sigma_{XY}^T U\}$, s.t. $U^T U = \mathbf{I}$ and $u_j^T \Sigma_{XX} u_j = 0$ with covariances Σ_{XX} and Σ_{XY} for $U = [u_1, \ldots, u_L], j = 1, \ldots, L-1$, and identity matrix $\mathbf{I}$.

Assuming the latent space is far smaller than one of the predictors, we can then partition the space generated by X into two disjoint subspaces such that $X = (X_1, X_2)$ spanned by relevant (X_1) and irrelevant variables (X_2). The component $w = [w_1, \ldots, w_L]$ can be obtained by adding an l_1 constraint in the optimization of SIMPLS such that

$$\max_{w} w^T M w \text{ s.t. } w^T w = \mathbf{I}, \ \|w\| \leq \lambda, \tag{6}$$

where $M = X^T Y Y^T X$ and λ is a parameter limiting the extent of sparsity.

```
Construct dataStore object
1. Extract and matching records from MIMIC III patient database
2. Initialize training and validation signal to functional segments X_i
3. Dynamic band separation to X_{b,i}
4. Sparse kernel transformation X_{b,i,k}
5. Synthize GPL X_{B+1,i}

Stage 1 dataLearner X_{b,i,k} ⟶ Y_i^l
        dataLearner::enet
        dataLearner::enpls
        dataLearner::glmm
        dataLearner::inv
        dataLearner::keras
        dataLearner::sgPLS
        dataLearner::tsensembler

Stage 2 dataCombiner: Y_i^l ⟶ Y_i^r
        dataCombiner::randomForest
        dataCombiner::xgboost
        dataCombiner::SPLS
```

FIGURE 9. The pseudo-code representing the computation object structure.

Similar to other sparsity algorithms, such as Lasso or e-net, a multi-fold cross-validation step is needed in the computation. We also follow the standard procedure to find related sparsity control parameters.

The two-stage computation steps and object construction are finally summarized in Fig. 9. The implementation is designed in a style of object-objected programming. Before being sent to the learning ensemble, a dataStore object is constructed to represent the data unit $X_{b,i,k}$ in sparse kernel transformation after extracting and matching records from MIMIC III patient database. The object dataLearner and dataCombiner are designed to accomplish stage-1 and -2 processes, respectively. The ensemble algorithm will choose the best learner and a regression model among the bag of candidates.

IV. SIGNAL RECONSTRUCTION AND ANALYSIS

The proposed algorithms have been tested on a publicly available MIMIC III database [51] of PhysioNet.com [52]. This multi-parametric dataset contains 25,328 admissions to intensive care units. A large number of testing waveforms were used to validate the algorithm. A large quantity of PPG/ECG waveform pairs was extracted for the experiment. There is no limit on the number of records we could use, but screening the waveforms with the selected diseases in the complex hospital information system and ICD-9 (international disease classification) code system was not easy. Of these pairs, 70% and 30% of data were used for training and testing, respectively.

From the MIMIC III database, we extracted 287 records without being diagnosed having heart disease. We also matched 60 acute myocardial infarction (AMI), 30 atrial fibrillation (AF), and 170 heart failure (HF) records in the dataset. According to the convention of the hospital registration system, each record represented a particular recording during the stay from one of the multiple admissions of a patient. Therefore, we followed the same managerial logic that ignored the patient number and concentrated only on each admission because different admissions might receive different ICD-9 codes. The recording lengths varied from a few seconds to several hours. We will not overuse a single patient and only kept a part of such a long record for keeping balanced sampling. The data structure in the experiment was divided into record, chunk, and segment. A segment is a basic unit with the bandwidth of the functional time series. A chunk contains 10∼50 segments, and a record consists of 5∼20 chunks. The part of recording outside the target range of chunks was discarded.

A semi-automatic pre-processing step was performed along with visual inspection to join multiple columns among patient subjectID, ICD9 code ranges for a group of diseases, admissionID, recordingID, and signal waveforms. Before the waveforms were entered for training, the records with all-zero elements or without complete 'PLETH'/'lead II' pair were excluded. Although our algorithm could accept a wide range of acquisition quality, flat zero signals still are unacceptable because they would mislead the algorithm. The high noise or irregular wave signals were preserved for testing our algorithm's robustness.

A. PREDICTION RESULTS IN EACH SRD BANDS

We iteratively employed a combination of learners in the first stage ensemble for each band in the experiments. The learners in the ensemble for this experiment were defined as [1, 2, 3, 4, 5, 6] = [t-l2, t-l1, w-l2, w-l1, dcnn, warp], for which represent [an ordinary generalized matrix inverse in l_2, an ordinary generalized matrix inverse in l_1, Lasso in l_2, Lasso in l_1, a 40-layer VGG19 model [53], and a waveform warping method], respectively. Many learners were excluded from the experiments because they did not perform well, either in the training or testing steps.

In Fig. 10 (a), the SRD filtered signals of low-band were smooth and congruent to each other. Therefore, the mapping in this band was easy and would guarantee the heart rate of the final transformation will be accurate.

In Fig. 10 (b), the mid-band of the SRD carried prominent signal information, and this band's accuracy dictated the quality of the final reconstructions. In Fig. 10 (c), in the high-band of the SRD, most of the coefficients should be zero.

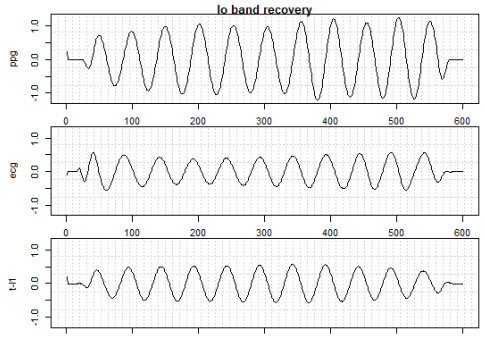

(a) low band

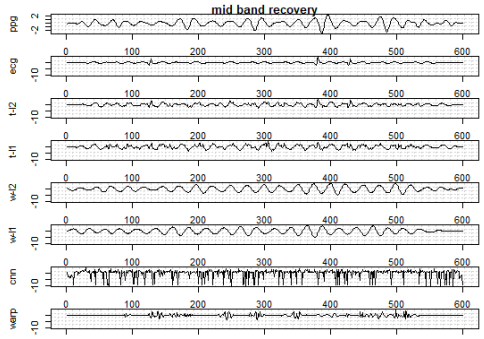

(b) mid band

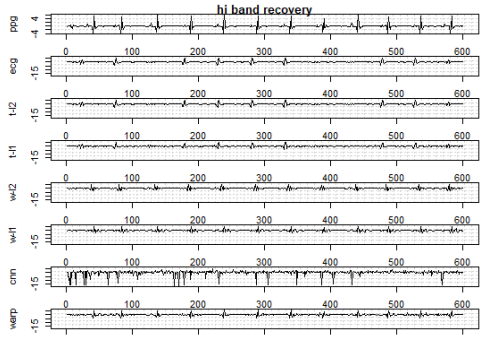

(c) high band

FIGURE 10. **(a) In the low-band, mapping is sufficiently stable when an ordinary generalized matrix inverse is used in the learner, (b) In the mid-band, different mapping methods in the learner yield various levels of mapping performance. (c) In the high-band, the property of sparsity dominates the mapping and therefore l_1 learners have better performance. (The learners are numbered as t-l2=1, t-l1=2, w-l2=3, w-l1=4, dcnn=5, warp=6.)**

The generative pulse locking for the QRS complex in this band also helped stabilize the quality of the mapping.

B. PREDICTION ACCURACY

Several metrics were adopted for evaluating performance, including standard ones, the relative root mean squared error (rrmse), and Pearson correlation coefficient (ρ). We also applied Kling–Gupta efficiency (KGE) values [54] to assess the goodness of fit for the similarity between two functional time series. Given the functionals of the simulated signal *sim* and observed signal *obs*, the statistics of *sim* and *obs* are

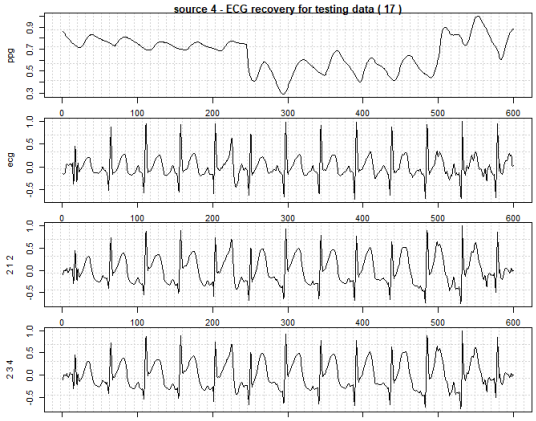

FIGURE 11. **The ECG signals were recovered from the source record set 4 and testing segment 17. The top two subgraphs showed the original PPGs and ECGs, and the third and fourth subgraphs showed the best ECG reconstruction using the appropriate learners (The learners are numbered as t-l2=1, t-l1=2, w-l2=3, w-l1=4, dcnn=5, warp=6.)**

prepared for the KGE measure. μ_{sim} and μ_{obs} are the means of *sim*. σ_{sim} σ_{obs} are the variances of *obs*.

The KGE are defined in Eq. (7).

$$\mathrm{KGE} = 1 - \sqrt{(r-1)^2 + \left(\frac{\sigma_{sim}}{\sigma_{obs}} - 1\right)^2 + \left(\frac{\mu_{sim}}{\mu_{obs}} - 1\right)^2}, \quad (7)$$

where r is the Pearson correlation between the two functionals *sim* and *obs*. The KGE value implies that the larger the KGE is, the better the fit will be.

Besides similarity, the dissimilarity between the simulated and all other non-target waveforms should be measured. Even though the simulation may not perfectly match the target, the simulation should not accidentally match any other targets. Therefore, we define a Kling–Gupta efficiency difference (KGED) by taking a uniform expectation E overall records in the dataset [30].

$$\mathrm{KGED} = \mathrm{E}_{\forall i}[\mathrm{KGE}_i - \max\{\mathrm{KGE}_j\}_{\forall j \neq i}]. \quad (8)$$

Positive values of KGED imply high goodness of fit for the specific targets.

The training result for the proposed ensemble approach was illustrated in Fig. 11. Based on the goodness-of-fit articulated in Table 2, the results of the prediction were demonstrated in the functional form. Even in the case of extremely poor acquisition quality of PPG, the predicted reconstruction still maintains robustness without losing statistical details.

The two best prediction results were shown in the third and fourth subgraphs of Fig. 11 using learners (2,1,2) and (2,3,4). The learners are numbered as t-l2=1, t-l1=2, w-l2=3, w-l1=4, dcnn=5, warp=6. The low-band in both cases was suitable for learner 2, which corresponds to t-l1 (the ordinary pseudo-inverse in l_1). For the mid-band, t1-l2 and w-l2 were equally good. For the high-band, t-l1 and w-l1 can perfectly preserve the sparsity property.

Stable results are obtained through our algorithm. Based on the prediction accuracy in Table 2, we find that the reconstructed ECG can perform disease diagnosis with

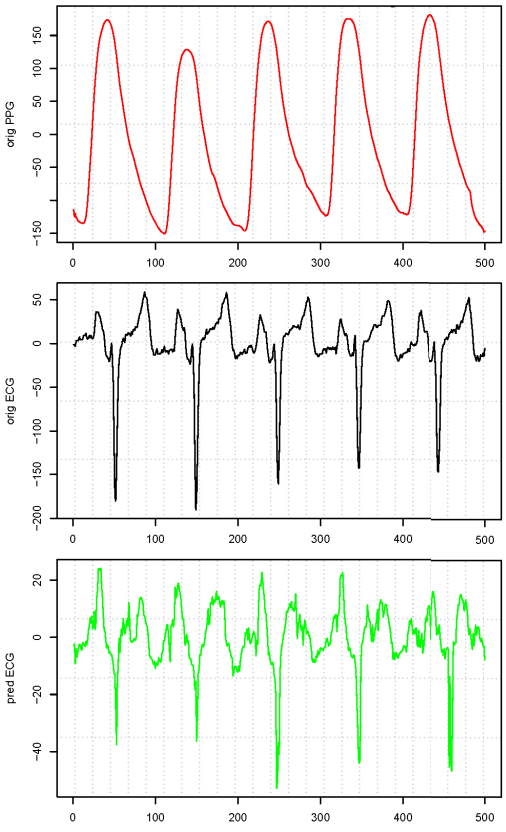

(a) AMI PPG

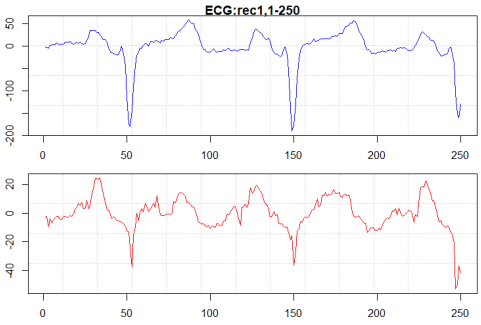

(b) zoom-in comparison

FIGURE 12. A validated reconstruction of an AMI ECG. Given an unseen PPG and ECG at the top 2 subgraphs of (a) (orig=original), we obtain the predicted ECG (pred=predicted) at the bottom subgraph. The subgraph (b) zoomed in on the details (2 sec.) of the predicted ECG (upper) and the original ECG (lower).

great accuracy. For patients with ICD-9 codes relating to AMI, AF, and HF, we obtained correctness rates of 85%, 80%, and 78%, respectively.

For comparison, in the individual learner, we also deployed a deep convolutional neural network (DCNN) in a well-known 40 layers VGG19 model [53]. As shown in Fig. 13, the results did not perform as well as our method, either in the training or testing data. From the subgraph, we can observe that the performance of VGG19 significantly deviated from other methods. The original PPG and ECG are in the first two

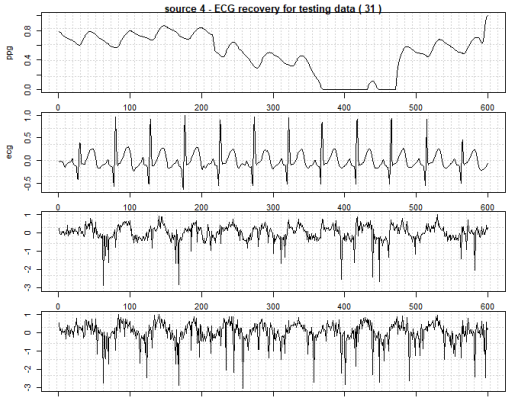

FIGURE 13. Comparison to other methods. A popular DCNN was used in the algorithm but the reconstructed signals did not perform as well as our method, compared to the results in Fig. 11. The first and the second subgraphs are the original PPG and ECG, respectively. The third (mid-band=w-l1,high-band=dcnn) and the fourth (mid-band=dcnn,high-band=dcnn) subgraphs are the DCNN prediction outputs.

subgraphs and the next two subgraphs show two samples of reconstructions by combinations of learners, which demonstrate an average reconstruction result.

In the subgraphs of Fig. 13, the third (mid-band=w-l1, high-band=dcnn) and the fourth (mid-band=dcnn,high-band=dcnn) were the outputs with DCNN learner. The reconstructions did not surpass the quality of other methods. A DCNN may not be a perfect choice in this application with time series contents.

The maximal similarity between the reconstructed and the original ECG occurred by using the methods SRD-GPL in l_2 and l_1, whose performance is superior in both training and testing data, compared to other methods, such as DCNN. The proposed learning model improves prediction accuracy (KGE) and specificity (KGED).

Our algorithm shows excellent results in avoiding overfitting, and the prediction is made specifically for the target ECG, according to the indication of KGED. Our goal of prediction satisfies two criteria: statistical error should be small for the unseen ECG, and should not be similar to any other ECG (the error difference between target and non-target waves should be significant).

C. DISCUSSIONS

Our results show the feasibility of mapping from PPG to ECG signals based on the theoretical basis of electro-fluid-mechanics and hemodynamics. The regularization in l_1 is rooted in the cellular activation dynamics.

The mapping results reveal that the low-band is relatively stable, the mid-band is informative for the waveform details, and the high-band is distinguishable for the similarity. We can spend less computation time in the low-band and still obtain a relatively stable prediction for the final mapping. We should spend most computation resources in the mid-band because the waveform details manifest in this band. Considering that

TABLE 2. Average prediction accuracy under four disease categories.

category	training rrmse	testing rrmse	diagnostic correctness	ρ	KGE	KGED
normal	.049	.283	.91	.88	0.82	5.78
AMI	.038	.302	.85	.81	0.63	3.36
AF	.029	.291	.80	.74	0.58	3.11
HF	.101	.314	.78	.65	0.55	3.25

rrmse=relative root mean squared error; ρ=Pearson correlation coefficient

KGE=Kling–Gupta efficiency; KGED=KGE difference; (The larger the better)

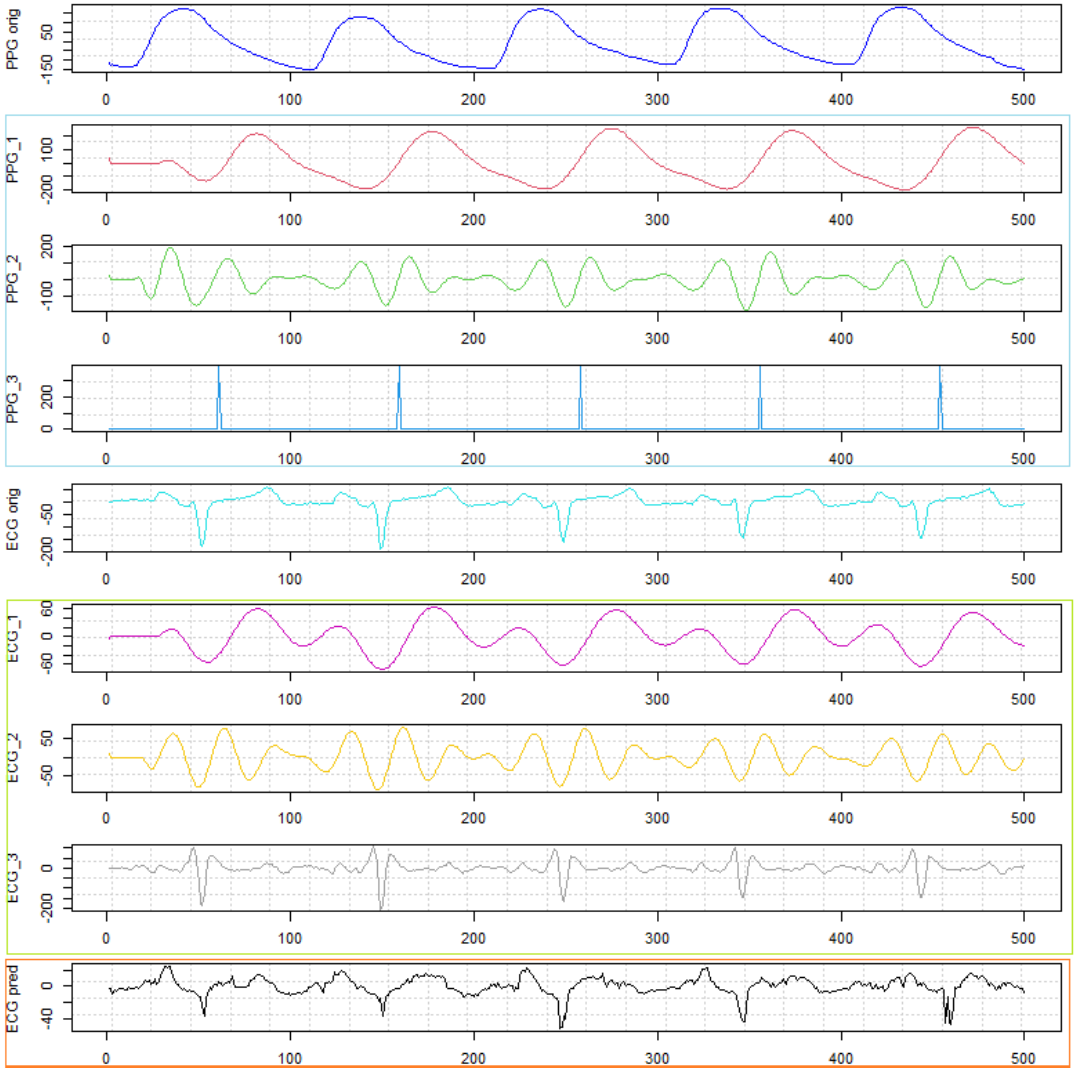

FIGURE 14. From top to the bottom, the original AMI PPG in (first) has been decomposed to 3-band (second)-(fourth), and the ECG in (fifth) has been decomposed to 3-band (sixth)-(eighth). Through the banded kernel ensemble, the final prediction of the ECG was shown in (ninth).

the QRS complex is the most distinguishable part of ECG, a conditioning step with generative pulses and a regularized l_1 penalization are effective in the computation of high-band. Using the trained model, we can quickly generate a high-fidelity ECG solely based on easy-to-measure PPGs.

We demonstrate our conversion result by acquiring the PPG from an AMI patient. The reconstruction result from our ensemble was shown in Fig. 14. Even taking from a low-quality PPG signal, we still can synthesize an almost identical ECG signal based on such limited conditions. For the

validation of our reconstruction of the AMI ECG, the original ECG signals are similar to the predicted ECG signal (Fig. 12 (a)). Given an unseen PPG and ECG at the top 2 subgraphs of (a) (orig PPG=original PPG, orig ECG=original ECG), we obtain the predicted ECG (pred ECG=predicted ECG) at the bottom subgraph. We zoom in on the details in the subgraph (b) (from point 1 to point 250, corresponding to 2 seconds in the sampling rate of 125 Hz) of the predicted ECG (upper) and the original ECG (lower). The reconstructed prediction preserves the features of the original ECG even in the AMI case.

D. LIMITATIONS AND FUTURE WORKS

This study tried to extract matched records from the MIMIC III database. Because the waveforms and disease codes were stored in separated data sources, the matching process was not easy. The record relations between two parts of sources were so complex, and therefore writing an automatic process is not reliable. Currently, the community still relies on visual inspection in getting disease codes for a waveform.

Future development can focus on improving prior distribution specifications and initial conditions. We will additionally construct empirical distribution for all error terms to be a basis of the prior distribution. The algorithm will be continuously improved and parallelized for better computational efficiency.

V. CONCLUSION

Low-quality PPG signals were mainly used to count heartbeats and measure SpO_2 and were difficult to be convinced for disease diagnoses. This study contributes to cardiology applications by upgrading such low-cost, ubiquitous devices to an operational level for regular medical practice. Based on electro-fluid-mechanics and haemodynamics in cardiology, our algorithm achieves a substantial accuracy in the reconstruction performance, and the calculated ECGs sufficiently replicate the waveform details of the original ECG signals.

We found that the inverse mappings are effective with the time-frequency band decomposition in the kernel space with l_1 norm. To yield the maximal similarity between the reconstructed and the original ECG, we apply the most suitable mapping method for each band, which also adapts dynamically to the cardiac activities. To address the challenge of ill-posed inverse mapping, we accommodate a generative pulse train synchronizing with the base frequency. The low-band in the mapping results is always stable, the mid-band is informative, and the high band is distinguishable. Here, we should focus on the inverse mapping of the mid-bands for superior waveform details.

Our method can alert suspicious cardiovascular symptoms at home and help a large population of high-risk, believed-healthy persons walks in doctors' offices before their cardiovascular health becomes irreversible. Our study demonstrates a stable and accurate mapping from PPG to ECG signals. Once ECG waveforms are derived from PPGs, many diseases, such as acute atrial infarction or arrhythmia, can be pre-screened in an ordinary surveillance camera.

REFERENCES

[1] (2021). Apple. *Apple Watch*. [Online]. Available: https://www.apple.com/watch/
[2] (2021). AliveCor. *AliveCor KardiaCare*. [Online]. Available: https://www.kardia.com/
[3] M. Garbey, N. Sun, A. Merla, and I. Pavlidis, "Contact-free measurement of cardiac pulse based on the analysis of thermal imagery," *IEEE Trans. Biomed. Eng.*, vol. 54, no. 8, pp. 1418–1426, Aug. 2007.
[4] K. Watanabe, T. Watanabe, H. Watanabe, H. Ando, T. Ishikawa, and K. Kobayashi, "Noninvasive measurement of heartbeat, respiration, snoring and body movements of a subject in bed via a pneumatic method," *IEEE Trans. Biomed. Eng.*, vol. 52, no. 12, pp. 2100–2107, Dec. 2005.
[5] J. Ogorevc, A. Podlesek, G. Gersak, and J. Drnovsek, "The effect of mental stress on psychophysiological parameters," in *Proc. IEEE Int. Symp. Med. Meas. Appl.*, May 2011, pp. 294–299.
[6] X.-R. Ding, Y.-T. Zhang, J. Liu, W.-X. Dai, and H. K. Tsang, "Continuous cuffless blood pressure estimation using pulse transit time and photoplethysmogram intensity ratio," *IEEE Trans. Biomed. Eng.*, vol. 63, no. 5, pp. 964–972, May 2016.
[7] W.-H. Tang, Y.-J. Chang, Y. J. Chen, and W.-H. Ho, "Genetic algorithm with Gaussian function for optimal P-wave morphology in electrocardiography for atrial fibrillation patients," *Comput. Electr. Eng.*, vol. 67, pp. 52–57, Apr. 2018.
[8] Y. Tao, Y. J. Chen, X. Fu, B. Jiang, and Y. Zhang, "Evolutionary ensemble learning algorithm to modeling of warfarin dose prediction for Chinese," *IEEE J. Biomed. Health Informat.*, vol. 23, no. 1, pp. 395–406, Jan. 2019.
[9] Y. A. Bhagat, P. Vcrdon, S. Avuthu, D. Parsons, M. Sussman, G. Wable, and R. Hugeneck, "Like kleenex for wearables: A soft, strong and disposable ECG monitoring system," in *Proc. IEEE Biomed. Circuits Syst. Conf. (BioCAS)*, Oct. 2018, p. 1.
[10] M. M. M. Nawawi, K. A. Sidek, A. K. Y. Dafhalla, and A. W. Azman, "Review on data acquisition of electrocardiogram biometric recognition in wearable smart textile shirts," *J. Phys., Conf.*, vol. 1900, no. 1, May 2021, Art. no. 012019.
[11] L. Wang, H. Zhang, K. C. Wong, H. Liu, and P. Shi, "Physiological-model-constrained noninvasive reconstruction of volumetric myocardial transmembrane potentials," *IEEE Trans. Biomed. Eng.*, vol. 57, no. 2, pp. 296–315, Feb. 2010.
[12] M. Courtemanche, R. J. Ramirez, and S. Nattel, "Ionic mechanisms underlying human atrial action potential properties: Insights from a mathematical model," *Amer. J. Physiol.-Heart Circulatory Physiol.*, vol. 275, no. 1, pp. H301–H321, Jul. 1998.
[13] M. P. Nash and A. V. Panfilov, "Electromechanical model of excitable tissue to study reentrant cardiac arrhythmias," *Prog. Biophys. Mol. Biol.*, vol. 85, nos. 2–3, pp. 501–522, Jun. 2004.
[14] Y. Rudy, "Noninvasive electrocardiographic imaging of arrhythmogenic substrates in humans," *Circulat. Res.*, vol. 112, no. 5, pp. 863–874, Mar. 2013.
[15] W.-H. Tang, W.-H. Ho, and Y. J. Chen, "Data assimilation and multi-source decision-making in systems biology based on unobtrusive Internet-of-Things devices," *Biomed. Eng. OnLine*, vol. 17, no. S2, pp. 35–47, Nov. 2018.
[16] Y. Tsaig and D. L. Donoho, "Extensions of compressed sensing," *Signal Process.*, vol. 86, no. 3, pp. 549–571, Mar. 2006.
[17] Q. Zhu, X. Tian, C.-W. Wong, and M. Wu, "ECG reconstruction via PPG: A pilot study," in *Proc. IEEE EMBS Int. Conf. Biomed. Health Informat. (BHI)*, May 2019, pp. 1–4.
[18] X. Tian, Q. Zhu, Y. Li, and M. Wu, "Cross-domain joint dictionary learning for ECG reconstruction from PPG," in *Proc. IEEE Int. Conf. Acoust., Speech Signal Process. (ICASSP)*, May 2020, pp. 936–940.
[19] H.-Y. Chiu, H.-H. Shuai, and P. C.-P. Chao, "Reconstructing QRS complex from PPG by transformed attentional neural networks," *IEEE Sensors J.*, vol. 20, no. 20, pp. 12374–12383, Oct. 2020.
[20] K. Vo, E. K. Naeini, A. Naderi, D. Jilani, A. M. Rahmani, N. Dutt, and H. Cao, "P2E-WGAN: ECG waveform synthesis from PPG with conditional Wasserstein generative adversarial networks," in *Proc. 36th Annu. ACM Symp. Appl. Comput.*, Mar. 2021, pp. 1030–1036.

[21] K. Qin, W. Huang, and T. Zhang, "Deep generative model with domain adversarial training for predicting arterial blood pressure waveform from photoplethysmogram signal," *Biomed. Signal Process. Control*, vol. 70, Sep. 2021, Art. no. 102972.
[22] A. Akbari, J. Martinez, and R. Jafari, "A meta-learning approach for fast personalization of modality translation models in wearable physiological sensing," *IEEE J. Biomed. Health Informat.*, vol. 26, no. 4, pp. 1516–1527, Apr. 2022.
[23] D. Martin-Martinez, P. Casaseca-de-la-Higuera, M. Martin-Fernandez, and C. Alberola-Lopez, "Stochastic modeling of the PPG signal: A synthesis-by-analysis approach with applications," *IEEE Trans. Biomed. Eng.*, vol. 60, no. 9, pp. 2432–2441, Sep. 2013.
[24] V. Duval and G. Peyré, "Sparse spikes super-resolution on thin grids II: The continuous basis pursuit," *Inverse Problems*, vol. 33, no. 9, Sep. 2017, Art. no. 095008.
[25] E. J. Candes and J. K. Romberg, "Signal recovery from random projections," *Proc. SPIE*, vol. 5674, pp. 76–87, Mar. 2005.
[26] R. G. Baraniuk and M. B. Wakin, "Random projections of smooth manifolds," *Found. Comput. Math.*, vol. 9, no. 1, pp. 51–77, 2009.
[27] Y. C. Eldar and M. Mishali, "Robust recovery of signals from a structured union of subspaces," *IEEE Trans. Inf. Theory*, vol. 55, no. 11, pp. 5302–5316, Nov. 2009.
[28] R. G. Baraniuk, V. Cevher, M. F. Duarte, and C. Hegde, "Model-based compressive sensing," *IEEE Trans. Inf. Theory*, vol. 56, no. 4, pp. 1982–2001, Apr. 2010.
[29] U. Beyaztas and Z. M. Yaseen, "Drought interval simulation using functional data analysis," *J. Hydrol.*, vol. 579, Dec. 2019, Art. no. 124141.
[30] M.-H. Lee and J. Y. Chen, "Precipitation modeling for extreme weather based on sparse hybrid machine learning and Markov chain random field in a multi-scale subspace," *Water*, vol. 13, no. 9, pp. 1241–1253, May 2021.
[31] A. Kovnatsky, M. M. Bronstein, X. Bresson, and P. Vandergheynst, "Functional correspondence by matrix completion," in *Proc. IEEE Conf. Comput. Vis. Pattern Recognit. (CVPR)*, Jun. 2015, pp. 905–914.
[32] Z. Zhang, "Photoplethysmography-based heart rate monitoring in physical activities via joint sparse spectrum reconstruction," *IEEE Trans. Biomed. Eng.*, vol. 62, no. 8, pp. 1902–1910, Aug. 2015.
[33] P. Fryzlewicz, S. Van Bellegem, and R. von Sachs, "Forecasting non-stationary time series by wavelet process modelling," *Ann. Inst. Stat. Math.*, vol. 55, no. 4, pp. 737–764, Dec. 2003.
[34] N. M. Pindoriya, S. N. Singh, and S. K. Singh, "An adaptive wavelet neural network-based energy price forecasting in electricity markets," *IEEE Trans. Power Syst.*, vol. 23, no. 3, pp. 1423–1432, Aug. 2008.
[35] H. Kim, Y. Kim, J. Kim, and E. C. Lee, "Method for restoring PPG signals using ECG correspondences and SVR," *Electron. Lett.*, vol. 49, no. 24, pp. 1518–1520, Nov. 2013.
[36] W.-H. Ho, J. Y. Chen, Y. Zhang, Y. Tao, and H.-W. Kuo, "Heart diseases detection from noisy recordings of smartphone devices," *J. Mech. Med. Biol.*, vol. 18, no. 4, pp. 1–16, Jun. 2018.
[37] F. Yao, H.-G. Müller, and J.-L. Wang, "Functional data analysis for sparse longitudinal data," *J. Amer. Stat. Assoc.*, vol. 100, no. 470, pp. 577–590, 2005.
[38] A. Antoniadis, E. Paparoditis, and T. Sapatinas, "Bandwidth selection for functional time series prediction," *Statist. Probab. Lett.*, vol. 79, no. 6, pp. 733–740, Mar. 2009.
[39] P. Vincent and Y. Bengio, "Kernel matching pursuit," *Mach. Learn.*, vol. 48, nos. 1–3, pp. 165–187, 2002.
[40] H. Zou and T. Hastie, "Regularization and variable selection via the elastic net," *J. Roy. Statist. Soc., B, Stat. Methodol.*, vol. 67, no. 2, pp. 301–320, 2005.
[41] E. J. Candes and T. Tao, "Decoding by linear programming," *IEEE Trans. Inf. Theory*, vol. 51, no. 12, pp. 4203–4215, Nov. 2005.
[42] E. J. Candès, J. Romberg, and T. Tao, "Robust uncertainty principles: Exact signal reconstruction from highly incomplete frequency information," *IEEE Trans. Inf. Theory*, vol. 52, no. 2, pp. 489–509, Feb. 2006.
[43] D. W. Marquardt and R. D. Snee, "Ridge regression in practice," *Amer. Statist.*, vol. 29, no. 1, pp. 3–20, 1975.
[44] C. B. García, J. García, M. M. L. Martín, and R. Salmerón, "Collinearity: Revisiting the variance inflation factor in ridge regression," *J. Appl. Statist.*, vol. 42, no. 3, pp. 648–661, Mar. 2015.
[45] P. Exterkate, P. J. F. Groenen, C. Heij, and D. V. Dijk, "Nonlinear forecasting with many predictors using kernel ridge regression," *Int. J. Forecast.*, vol. 32, no. 3, pp. 736–753, Jul. 2016.
[46] I. Goodfellow, J. Pouget-Abadie, M. Mirza, B. Xu, D. Warde-Farley, S. Ozair, A. Courville, and Y. Bengio, "Generative adversarial nets," in *Proc. Adv. Neural Inf. Process. Syst.*, 2014, pp. 2672–2680.
[47] H. Chun and S. Keleş, "Sparse partial least squares regression for simultaneous dimension reduction and variable selection," *J. Roy. Stat. Soc. Stat. Methodol. B*, vol. 72, no. 1, pp. 3–25, 2010.
[48] G. Zhu and Z. Su, "Envelope-based sparse partial least squares," *Ann. Statist.*, vol. 48, no. 1, pp. 161–182, Feb. 2020.
[49] S. de Jong, "SIMPLS: An alternative approach to partial least squares regression," *Chemometrics Intell. Lab. Syst.*, vol. 18, no. 3, pp. 251–263, Mar. 1993.
[50] I. S. Helland, "Model reduction for prediction in regression models," *Scandin. J. Statist.*, vol. 27, no. 1, pp. 1–20, Mar. 2000.
[51] A. E. Johnson, T. J. Pollard, L. Shen, H. L. Li-Wei, M. Feng, M. Ghassemi, B. Moody, P. Szolovits, L. A. Celi, and A. G. Mark, "MIMIC-III, a freely accessible critical care database," *Sci. Data*, vol. 3, May 2016, Art. no. 160035.
[52] A. L. Goldberger, L. A. N. Amaral, L. Glass, J. M. Hausdorff, P. C. Ivanov, R. G. Mark, J. E. Mietus, G. B. Moody, C.-K. Peng, and H. E. Stanley, "PhysioBank, PhysioToolkit, and PhysioNet: Components of a new research resource for complex physiologic signals," *Circulation*, vol. 101, no. 23, pp. e215–e220, Jun. 2000.
[53] K. Simonyan and A. Zisserman, "Very deep convolutional networks for large-scale image recognition," 2014, *arXiv:1409.1556*.
[54] S. Pool, M. Vis, and J. Seibert, "Evaluating model performance: Towards a non-parametric variant of the Kling-Gupta efficiency," *Hydrol. Sci. J.*, vol. 63, nos. 13–14, pp. 1941–1953, Oct. 2018.

WEN-HSIEN HO received the B.S. degree in marine engineering from the National Taiwan Ocean University, in June 1991, the B.S. degree in industrial and information management from the National Cheng-Kung University, in June 1998, and the M.S. degree in mechanical and automation engineering and the Ph.D. degree in engineering science and technology from the National Kaohsiung First University of Science and Technology, Taiwan, in June 2002 and January 2006, respectively. From September 1991 to July 2006, he was an Engineer of the Design Department, CSBC Corporation, Taiwan. He is currently a Professor with the Department of Healthcare Administration and Medical Informatics, Kaohsiung Medical University, Taiwan. His research interests include intelligent systems and control, computational intelligence and methods, robust control, and quality engineering.

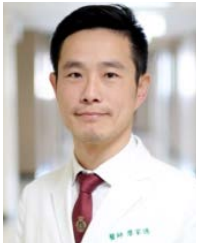

CHIA-TE LIAO received the M.Sc. degrees from the London School of Hygiene and Tropical Medicine and the London School of Economics and Politics and the M.D. degree from Taipei Medical University. He is currently pursuing the joint Ph.D. degree with the National Cheng Kung University, Taiwan, and Leuven University, Belgium. He is currently a Cardiologist and an Assistant Professor with the Chi-Mei Medical Center. He has several publications, including books and more than 30 SCI papers. His research interests include clinical trial, cardiological epidemiology, health economics, health technology assessment, artificial intelligence in medicine, public health, health policy, and quality improvement.

YENMING J. CHEN received the Ph.D. degree in systems science and mathematics from Washington University, St. Louis, USA, in 1998. He is currently a Distinguished Professor with the Information Management Department, National Kaohsiung University of Science and Technology, Taiwan. He is the author of several books, patents, and more than 75 SCI/SSCI articles. His research interests include the IoT/AI, sound/spectrum technologies, fault detection, precision medicines, and medical computations.

KAO-SHING HWANG received the M.M.E. and Ph.D. degrees in electrical and computer engineering from Northwestern University, Evanston, IL, USA, in 1989 and 1993, respectively. He was with the National Chung Cheng University, Taiwan, from 1993 to 2011, where he was the Deputy Director of the Computer Center, from 1998 to 1999, the Chairman of the Electrical Engineering Department, from 2003 to 2006, and the Director of the Opti-Mechatronics Institute, from 2010 to 2011. He is a Distinguished Professor/A.S.E. Group Chair Professor of the Electrical Engineering Department, National Sun Yat-sen University. He is also an Adjunct Chair Professor of Kaohsiung Medical University, Taiwan; a Distinguished Chair Professor of the National Formosa University, Taiwan; and a Visiting Chair Professor of the Department of Computer Engineering, Northwestern Polytechnic University, Xi'an, China. His research interests include methodologies and analysis for various intelligent systems, visual servoing, and reinforcement learning for medical aid systems and robotic applications. He is a fellow of the Institution of Engineering and Technology (FIET). He received the MOST 2020 Outstanding Research Award, Taiwan.

YANYUN TAO received the Ph.D. degree from the East China University of Science and Technology. He was a Postdoctoral Researcher with Shanghai Jiaotong University. He is an Associate Professor with Soochow University. He has published 17 SCIE articles in machine learning for medical application. He was supported by the "Talent of Colleges and Universities in Suzhou." He was also supported by the National Natural Science Foundation of China; the China Postdoctoral Science Foundation; and the State Key Laboratory of New Software Technology, Nanjing University. His research interests include computational intelligence, machine learning, and biomedical engineering. He is a member of the Young Scientist Association of the China Artificial Intelligence Society. He received the Second Prize of Scientific and Technological Progress from the Suzhou Computer Society.